SAND2019-5060J

Dynamic recrystallization suppresses ductile rupture in high-purity aluminum

Philip Noell, Ryan Sills, Brad Boyce

Key Words: Fracture, void nucleation, dynamic recrystallization, vacancy condensation, cavitation

Abstract

Previous studies of rupture in high-purity face-centered-cubic (FCC) metals, primarily aluminum (Al), concluded that 2nd-phase particles are necessary for cavitation. A recent study of Ta, a body-centered-cubic (BCC) metal, demonstrated that voids nucleate readily at deformation-induced dislocation boundaries. These same features form in Al during plastic deformation. This study investigates why void nucleation was not previously observed at these dislocation boundaries. We demonstrate that void nucleation is impeded in Al by room-temperature dynamic recrystallization (DRX), which erases these boundaries before voids can nucleate at them. If dislocation cells reform after DRX and before specimen separation by necking, voids nucleate at them. These results indicate that defect/defect interactions can create void-nucleation sites in inclusion-free FCC materials that deform by slip.

1 Introduction

Before 1950, the question of how and where voids nucleate during ductile rupture was hotly debated. Several researchers proposed that voids nucleated at the head of blocked slip bands by a cleavage-like mechanism [1, 2], while others hypothesized that voids formed by dislocation reactions [3-5]. The invention of the scanning electron microscope enabled the discovery by Tipper and others [6, 7] that voids nucleate at second-phase particles. Based on this discovery, Cottrell hypothesized that "if such particles were not present, the specimen would pull apart entirely by the inward growth of the external neck, giving nearly 100% reduction in area" [5]. Several critical experiments on high-purity face-centered-cubic (FCC) metals, primarily aluminum (Al), strongly supported this conclusion [7-12]. For example, using aluminum, Chin *et al.* [10] observed that the dimple density on the fracture surface decreased with increasing sample purity. In the extreme case, zone-refined (approximately 99.999% Al) aluminum failed by necking to a chisel point rather than by cavitation [10]. Similar trends were reported in high-purity lead (Pb) [9], though the resolution of the characterization techniques used in those studies was likely insufficient to detect voids smaller than 10 μm. These results have led to the conclusion that generalized void nucleation does not occur in bulk, particle-free FCC metals that deform by slip [13-15].

In contrast, Boyce *et al.* [16] observed that high-purity tantalum (Ta), a body-centered-cubic (BCC) metal, failed in a ductile manner by void nucleation, growth, and coalescence. Subsequent analysis showed that voids

in Ta nucleated at deformation-induced dislocation boundaries, *i.e.* dislocation cell walls and cell block boundaries [17]. The same microstructural features also form in FCC metals that deform by slip, including Al [18, 19]. These observations raise an important question: why is void nucleation at dislocation boundaries suppressed in Al and, by extension, other FCC metals? It is possible that the relative ease of slip in FCC metals compared to BCC metals suppresses void nucleation at dislocation boundaries. However, the recent observation that the dimple-density on the fracture surface of high-purity Al specimens depended on grain size [20] suggests that other factors may also influence void nucleation in FCC metals.

In light of the recent observations of void nucleation at dislocation boundaries in BCC metals, the present study reexamines void nucleation in particle-free FCC metals. Al was chosen as the model material because of the extensive use of this material in early studies of void nucleation in particle-free materials. The following questions are addressed in this study:

1. Are there conditions under which voids nucleate in particle-free Al? If so, where do these voids nucleate?
2. What mechanism(s) prevent void nucleation in high-purity Al?
3. Why does dimple density on the fracture surface depend on purity?

The groundwork for a detailed study on void nucleation was laid by first examining the relationship between microstructure, purity, and void nucleation in Al wire materials of different purities. These experiments informed a subsequent examination of damage progression in a high-purity Al sheet material.

2 Materials and Methods

To observe the relationship between purity and void nucleation, an initial series of tests were performed on wire materials having nominal purities between 99.9% and 99.999% Al. Based on the groundwork laid by these experiments, a more detailed investigation was subsequently performed on an Al sheet material having a nominal purity of 99.99% Al. All materials were acquired from ESPI metals (Ashland, Oregon). The composition of each material was assessed independently using inductively coupled plasma mass spectroscopy [21]. The composition of the Al materials in parts per million (ppm) by volume are listed in Table 1. The purity of each material is abbreviated in this study as the number of nines of aluminum in the material, *e.g.* 99.9% aluminum is abbreviated as 3N-Al ("three nines aluminum"). The diameter of all three Al wires was 1.27 mm and the as-received thickness of the Al sheet was 2.07 mm.

Table 1: A list of the materials tested in this study and the form factor of each specimen is provided. The manufacturer's listed purity of each material is abbreviated as the number of nines of aluminum in the material, e.g. *3N-Al is 99.9% Al. The ppm by volume of trace impurities in each material are also listed. Based on these data, the measured purity of each material is provided as the % of Al.*

Material	Geometry	Mg	V	Cu	Zn	Ti	Ga	Fe	Si	%Al

3N-Al	Wire	14	3	6	30	182	246	416	146	99.9
4N-Al	Wire	14	<1	23	16	5	2	42	21	99.99
5N-Al	Wire	7	3	2	<1	4	1	1	1	99.999
4N-Al	Sheet	5	3	10	10	3	1	40	23	99.99

The as-received microstructures of these four materials were characterized using electron channeling contrast imaging (ECCI) with a Zeiss Supra 55VP field emission scanning electron microscope (SEM). Grain sizes were measured with the lineal intercept method [22]. Grains in all of the wire materials had dimensions of ~10 μm along the drawing direction and ~2 μm along the radial direction. Grains in the as-received 4N-Al sheet material were equiaxed, with an average diameter of 110 μm. Second-phase particles ranging from 0.2 to 5 μm were observed in the 3N-Al wire material. Energy dispersive X-ray spectroscopy (EDS) analysis of these particles demonstrated that they were composed of Silicon (Si) and Oxygen (O), which suggests that they were SiO_2 particles. These particles will thus be referred to as SiO_2 particles in this study. No second-phase particles or inclusions were identified in the 4N-Al and 5N-Al wire materials or the 4N-Al sheet material. EBSD data from the as-received microstructure of the 4N-Al material is shown in Figure 1**Error! Reference source not found.** (analysis methodology discussed below). These data indicate that this material contained residual dislocation substructures from cold working.

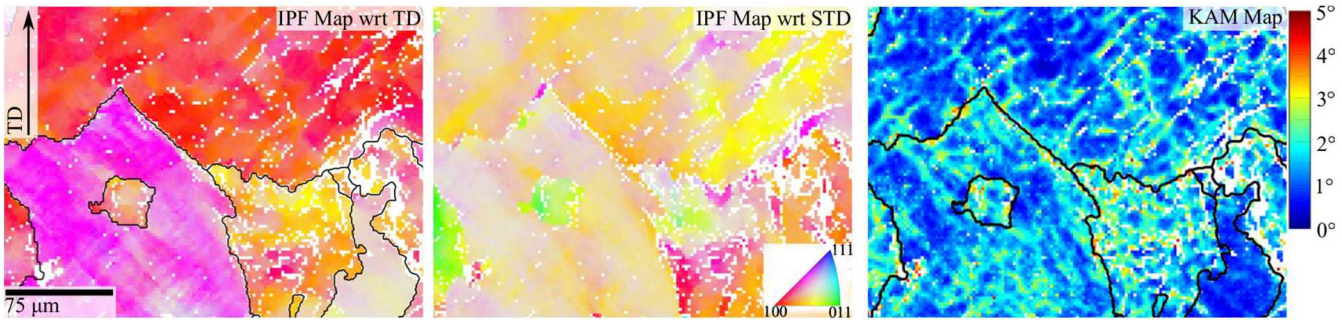

Figure 1. ***EBSD data from the grip region of a 4N-Al sheet specimen are plotted as inverse pole figure (IPF) maps colored with respect to the TD and STD and as a kernel average misorientation (KAM) map. Black lines overlaid on the IPF map colored with respect to the TD and KAM map highlight grain boundaries with misorientations of 5° or more across them.***

Specimens of all materials were tested in uniaxial tension with a servohydraulic machine using a constant cross-head displacement rate of 0.127 mm/s, corresponding to pre-necking strain rates of ~10^{-3} s^{-1} for wire specimens and ~10^{-2} s^{-1} for the sheet specimen. This small difference in strain rate between the wire and sheet specimens is considered negligible and has very little effect on stress-strain behavior [23]. Tensile specimens of the wire materials were cut from the wire spools and clamped in pneumatic grips with a wire length of approximately 100 mm between the grips. The primary axes of wire specimens are defined as the tensile direction (TD), which was parallel to the wire-drawing direction, and perpendicular to the radial direction (RAD). Specimens with

hourglass-shaped gauge regions having the same geometry as those used by Noell *et al.* [17] were fabricated from the sheet material using waterjet cutting with a minimum gauge width of 2.79 mm and an overall gauge length of 8.47 mm. Specimens retained the as-rolled sheet thickness of 2.07 mm. The primary axes of sheet specimens are defined as the TD, the long transverse direction (LTD), and the short transverse direction (STD). The STD was parallel to the sheet thickness. Tensile tests were either conducted until specimen rupture or were interrupted after the specimen reached its ultimate tensile strength (UTS) but before final fracture. In the latter case, the test was interrupted when the load carried by the specimen dropped from the UTS to a predetermined percentage of the UTS.

Strain measurements were performed for the 4N-Al sheet material using stereoscopic digital image correlation (DIC). As discussed in the results, the specimen necked significantly before fracture. To measure the average strain across the neck rather than across the entire gauge region, strain was measured from DIC data using a 0.7 mm virtual extensometer placed across the neck. A plot of engineering stress *versus* engineering strain for a 4N-Al sheet material elongated to failure are provided in Figure 4. Strain measurements were not made for the wire materials.

Fracture surfaces were evaluated in the SEM. Fractured specimens were subsequently mounted, ground to the midplane, and polished using 0.05 μm colloidal silica for extended periods to observe the midplane cross-section. Similarly, specimens that were interrupted before final fracture were ground to the midplane and subsequently polished. For sheet specimens, the TD-LTD plane, *i.e.* the plane normal to the STD, was examined. Wire specimens were sectioned along a plane parallel to the TD. In addition to SEM images, electron backscatter diffraction (EBSD) data were collected from polished samples using Oxford HKL AZtec™ [24] software. These data were subsequently processed using MTEX, [25] an extension for MATLAB. Kernel average misorientation (KAM) was calculated from these EBSD data using the misorientation between each pixel and its nearest neighbors. The lower bound of the geometrically necessary dislocation density in deformed samples was estimated from EBSD data with the method presented by Pantleon [26] as implemented in MTEX [25].

3 Results

3.1 Failure in the Al wire materials

To study the relationship between purity and void nucleation, specimens of the three wire materials were elongated to failure. Macrofractographs of these fractured specimens are provided in Figure 2. These results are analogous to those of Chin *et al.* [10]: the number of dimples on the fracture surface decreased with increasing purity until, for the highest purity wire material, specimens necked to a chisel point. However, high-magnification images of the fracture surface of the 5N-Al wire revealed a few, small (~2 μm) dimples. Several of these are shown in the inset in Figure 2c. These dimples indicate that voids nucleated shortly before final rupture. ECC images of the midplane cross-section of fractured specimens of each of the wire materials are also provided in Figure 2. The cross-section in Figure 2a shows that, in the 3N-Al wire material, voids nucleated

throughout the necked gauge region at SiO_2 particles. The 3N-Al material thus provides a useful example of void nucleation by conventional particle-based mechanisms. In the 4N-Al material, voids were localized to a narrow band within ~5 μm of the failure plane. A few such voids are highlighted in the inset in Figure 2b. No voids were identified in midplane cross section of the fractured 5N-Al wire.

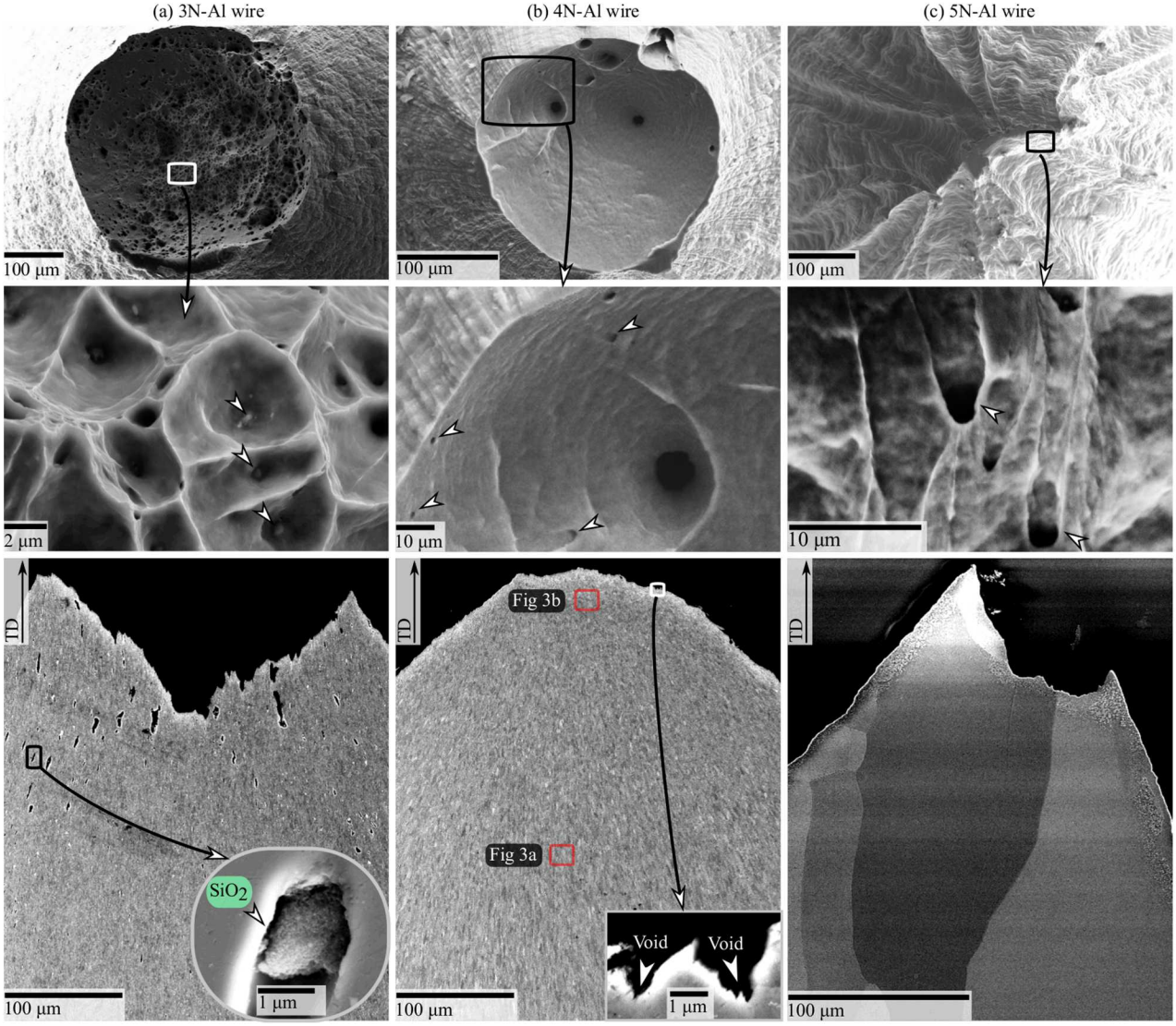

Figure 2. ***Images of fractured (a) 3N-Al, (b) 4N-Al, and (c) 5N-Al wires are shown. The upper row shows macrofractographs of fractured specimens of each material. The middle row shows high magnification images of the fracture surfaces of each material. Arrows in (a) highlight SiO_2 particles at the base of dimples, (b) small dimples on the fracture surface, and (c) dimples on the fracture surface. The lower row shows ECCI images of the midplane cross-section of fractured specimens of each material. Insets highlight important microstructural features: (a) shows a void that nucleated at a SiO_2 particle in the 3N-Al wire and (b) shows voids at the fracture surface of the 4N-Al wire.***

Significant differences were observed between the as-received and deformed microstructures of the 5N-Al wire. Instead of being heavily deformed, the ECC images in Figure 2c indicate that grains near the fracture surface of

the 5N-Al wire had low dislocation content. This difference is characteristic of dynamic recrystallization (DRX). Discontinuous DRX is known to occur in high-purity Al during room-temperature deformation [27, 28]. As Figure 2c shows, grains in this material were significantly larger after DRX than in the as-received material. This suggests that deformation may have enhanced the growth rate of recrystallized grains, either by causing secondary recrystallization [29] or dynamic abnormal grain growth [30-32]. Regardless of mechanism, grains near the fracture surface of the 5N-Al wire were, on average, at least an order of magnitude larger than those in the as-received material.

To determine if DRX also occurred during deformation of the 4N-Al wire, EBSD data were collected from the microstructure near the fracture surface and from the microstructure approximately 200 μm from the fracture surface. Reduction in area measurements at these two locations indicate that they underwent true strains of approximately 3.3 and 1.7, respectively. These EBSD datasets are plotted as inverse pole figure (IPF) maps in Figure 3. Texture and morphological differences were observed between grains in these two regions of the microstructure. Grains far from the fracture surface were elongated along the tensile axis and had a strong ⟨111⟩ fiber parallel to the TD typical of heavily deformed FCC metals [33]. In contrast, grains near the fracture surface were equiaxed and had a random texture. The most logical explanation for these differences is that DRX occurred in the local vicinity of the failure surface where the strain levels were largest. No evidence of DRX was observed in the 3N-Al wire material.

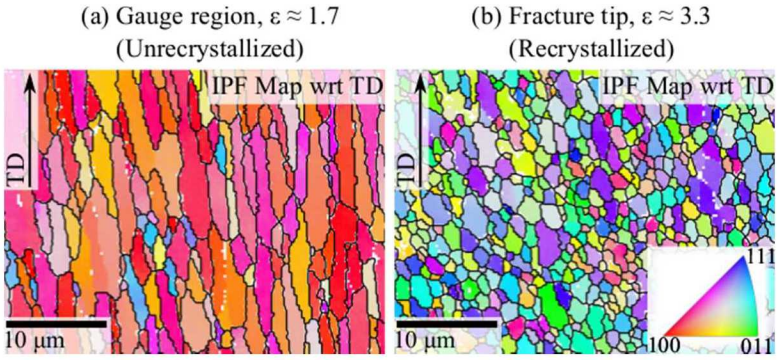

Figure 3. ***EBSD data from the microstructure in the 4N-Al wire in the (a) unrecrystallized gauge region ~200 μm from the fracture surface, and (b) recrystallized gauge region ~20 μm from the fracture surface are provided. These data are plotted as IPF maps colored with respect to the TD. The areas of the microstructure from which these data were collected are highlighted in Figure 2b. Black lines overlaid on the IPF maps highlight grain boundaries with misorientations of 5° or more across them.***

3.2 Failure in the Al sheet material

The initial tests on Al wire materials demonstrated that void nucleation was limited in the Al wire materials that

dynamically recrystallized. This observation motivated a detailed investigation of the failure process in high-purity Al. These tests were performed on a 4N-Al sheet material, which is more conducive to interrupted testing and *in-situ* strain measurements than the wire materials. To this end, a 4N-Al sheet specimen was elongated to failure and subsequently characterized. A plot of engineering stress *versus* engineering strain for this specimen is shown in Figure 4. An image of the fracture surface of this specimen is provided in Figure 5a. An ECC image of the midplane cross-section of this fracture surface is provided in Figure 5b. The sheet specimen failed by void nucleation, growth, and coalescence. One of these voids can be seen in the ECC image in Figure 5b.

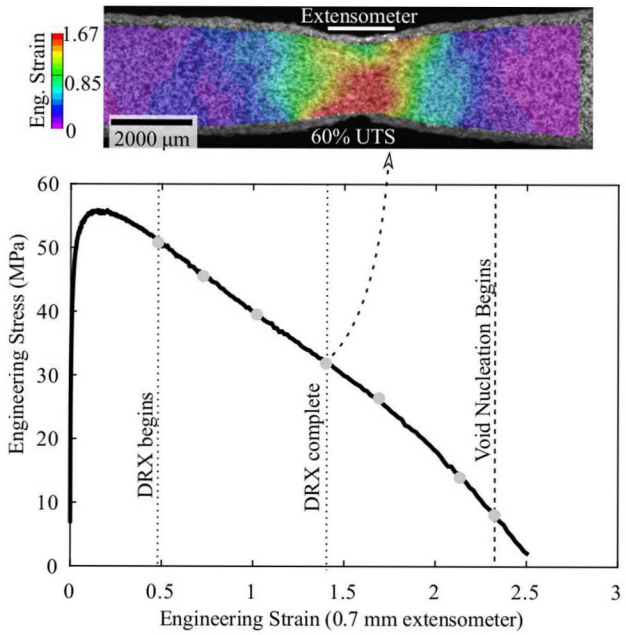

Figure 4. ***Engineering stress* versus *engineering strain data from a tensile test of the 4N-Al sheet material are presented. Gray dots on the plot denote where deformation of seven other 4N-Al tensile specimens was interrupted. To illustrate the size of the extensometer relative to the neck, an optical image overlaid with DIC data is shown above this plot. This image was taken at 60% of the UTS.***

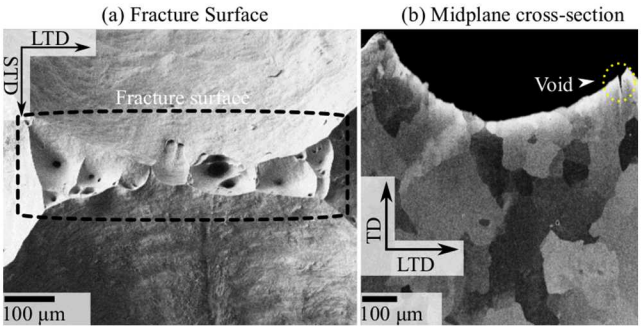

Figure 5. ***An image of the fracture surface of a 4N-Al sheet specimen is shown in (a). An ECC image of a midplane cross section of this specimen is shown in (b).***

The microstructure in the necked gauge region was significantly different from that outside the neck. This can be seen in the ECC image provided in Figure 6. Grains near the fracture surface appear relatively dislocation-free compared to those outside the necked gauge region. EBSD data also suggested that grains near the fracture surface are relatively dislocation-free, even compared to the as-received material. EBSD data collected from the necked gauge region are presented in Figure 7 as IPF maps and a KAM map. The average grain size of the material near the fracture surface, measured using these EBSD data, was 102 μm. Compared to the as-received material (see Figure 1), the KAM map in Figure 7c suggests that grains near the fracture surface were relatively dislocation free. It is thus concluded that DRX occurred in this material.

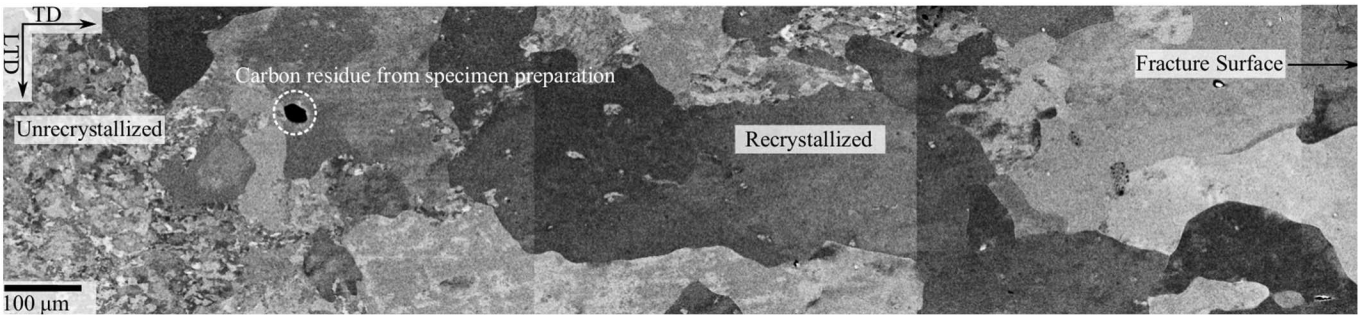

Figure 6. ***An ECC image of the material below the fracture surface of the 4N-Al sheet material is shown.***

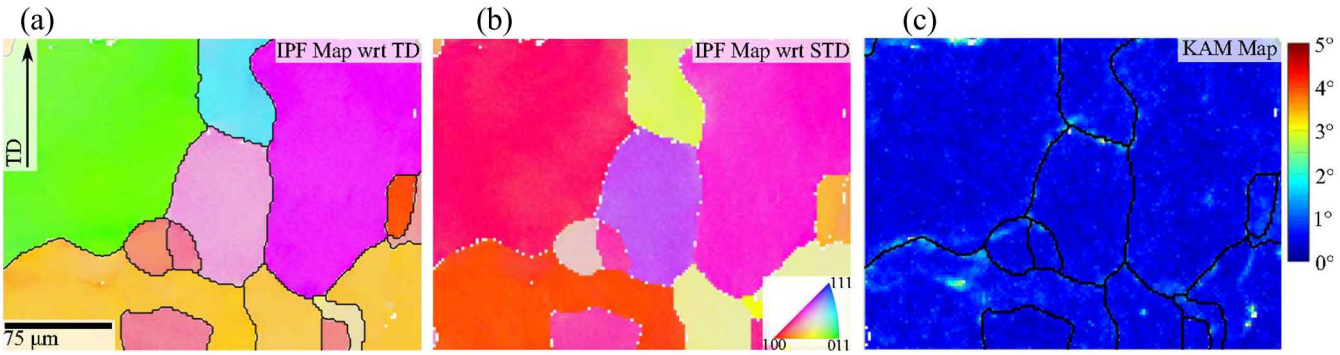

Figure 7. ***EBSD data from the microstructure near the fracture surface of a 4N-Al sheet specimen are plotted as IPF maps colored with respect to the TD and STD and as a KAM map. Black lines overlaid on (a) and (c) highlight grain boundaries with misorientations of 5° or more across them.***

To investigate when DRX occurred in this material, seven specimens were interrupted after the onset of necking, when the forces had dropped to 90%, 80%, 70%, 60%, 50%, 30%, and 15% of the UTS. The specimens were cross-sectioned and imaged to characterize the underlying microstructure. Using ECC images, two recrystallized grains were identified in the specimen interrupted at 90% UTS. By 60% UTS, all of the grains in the diffuse neck appeared to be recrystallized. Based on these results, the beginning and end of DRX are indicated on the plot in Figure 4.

To determine when void nucleation began, the center of the necked gauge region of each of these seven specimens was inspected. Voids were only observed in images of the necked gauge region of the specimen interrupted at 15% of the UTS. The approximate engineering stress and engineering strain when void nucleation began in this material is thus denoted on the plot in Figure 4.

To understand the microstructural features associated with void nucleation in this material, the midplane cross-section of the specimen interrupted at 15% of the UTS was inspected. A low-magnification ECC image of the midplane cross-section of this specimen is provided in Figure 8a. A few of the voids observed on this cross section are highlighted. EBSD and high-magnification ECC images were used to determine the microstructural origin of these voids. A high-magnification ECC image of one of these voids is provided in Figure 8b. EBSD data from the microstructure around this void, collected with a step size of 50 nm, are plotted as a band contrast (BC) map in Figure 8c and an IPF map colored with respect to the STD in Figure 8d. These data demonstrate that the void did not intersect a grain boundary within the plane examined. Instead, it was associated with a dislocation boundary. The dislocation boundaries within the grains near this void can be seen both within the ECC image and the BC map. A sketch of the dislocation boundaries near this void is provided in Figure 8e. The average misorientations across these boundaries and the closest grain boundary are labelled in this sketch. These data show that the void was associated with a low-angle dislocation boundary, likely a dislocation cell wall.

Similar analysis of another void in this specimen demonstrated that it was also associated with a low-angle dislocation boundary.

Using the method described by Pantleon [26], the EBSD data collected near these incipient voids were used to estimate the lower bound of the geometrically necessary dislocation (GND) density in the vicinity of these voids for the 50 nm stepsize used. The average GND density in the microstructure around both voids was ~10^{14} m^{-2}, and the average GND density of dislocation boundaries was ~10^{15} m^{-2}.

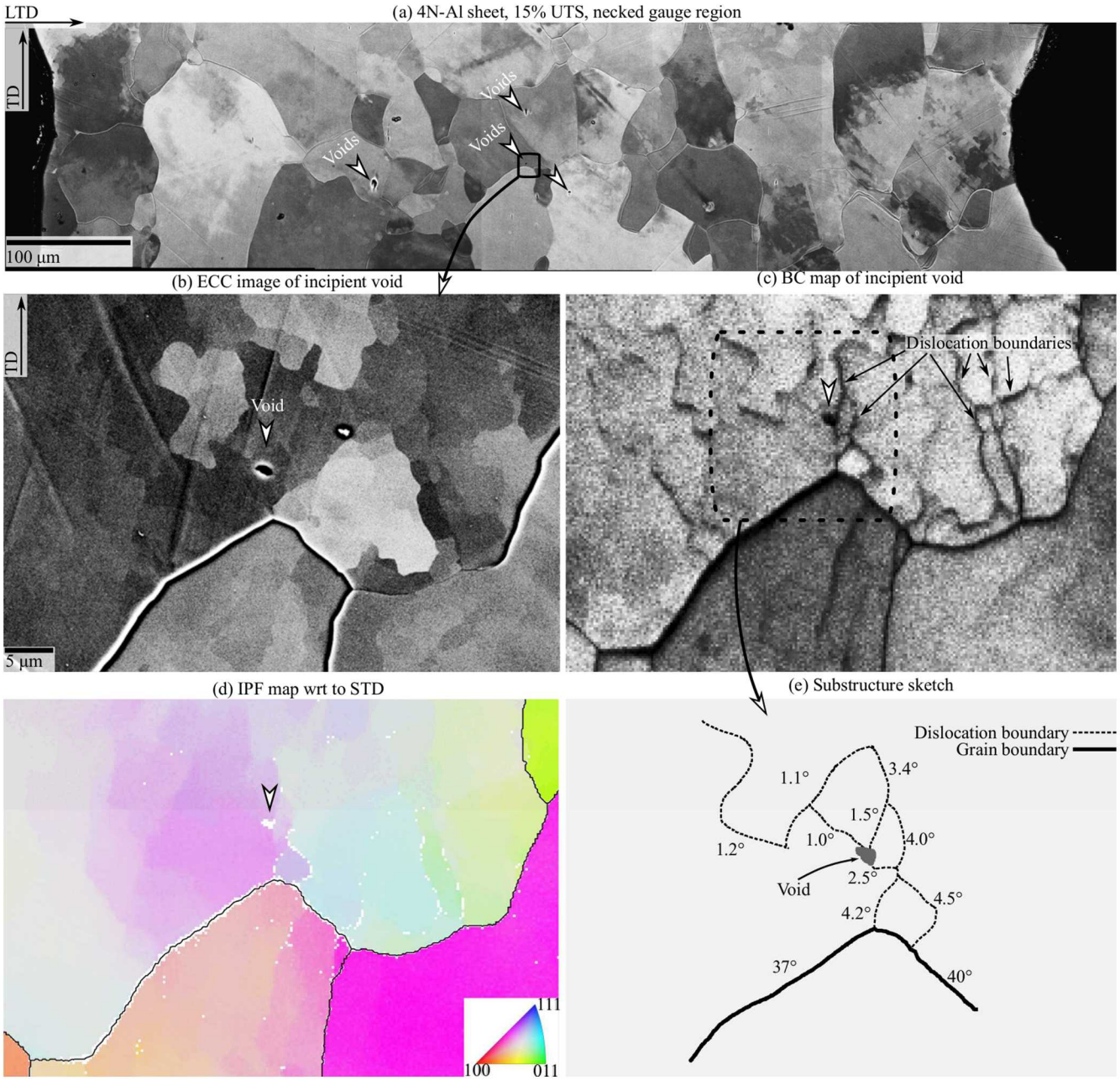

Figure 8. ***An ECCI image of the center of the necked gauge region of a 4N-Al sheet specimen interrupted at 15% of the UTS is shown in (a). A few of the voids and slip bands observed in this image are highlighted. A high-magnification ECCI image of the microstructure around one of the voids in (a) is shown in (b). EBSD data from the microstructure around this void are presented as (c) a pattern quality (band-contrast) map and (d) an IPF colored with respect to the STD. Black lines overlaid on the map in (d) delineate grain boundaries. The sketch in (e) illustrates some of the dislocation boundaries and grain boundaries around this void and the misorientations across them.***

4 Discussion

4.1 Void nucleation in particle-free Al

The present study demonstrates that voids in particle-free Al materials nucleate at dislocation boundaries. This is consistent with prior observations in BCC metals, where it was observed that voids nucleated exclusively at dislocation boundaries [17]. It is thus reasonable to conclude that void nucleation in metals that deform by slip depends on establishing a dislocation substructure consisting of dislocation boundaries. However, in high-purity Al, the DRX that occurs during plastic deformation erases the dislocation substructure critical to void nucleation. Void nucleation is then delayed until these boundaries reform. Hence, in particle-free Al, DRX suppresses void nucleation by annihilating dislocation boundaries.

These insights show that FCC metals are not uniquely resistant to void nucleation. Rather, void nucleation appears to be controlled by the same microstructural features in BCC and FCC metals that deform by slip. It is likely that the limited void nucleation observed in Pb can also be attributed to the effects of room-temperature DRX, since this is known to occur in Pb [34]. Both the creation and persistence of dislocation boundaries are thus essential to void nucleation in particle-free metals.

This conclusion implies that voids would nucleate readily in high-purity Al if DRX did not occur and dislocation boundaries were correspondingly allowed to form. DRX can be suppressed in this material by testing at temperatures below the recrystallization temperature, which Haessner *et al.* [35] estimated to be between -40° and 10° C. Although such cryogenic tests were not performed in this study, Chin *et al.* observed that the same high-purity Al samples that failed without voids at room temperature failed by void coalescence at -230° C [10]. This result further suggests that void nucleation would occur readily in Al if DRX did not occur.

One key question remains: why did the dimple density on the fracture surface and the competition between void coalescence and necking to a point in the Al wire materials depend on purity for the particle-free 4N and 5N-Al materials? As Figure 2 shows, the 4N-Al wire failed by void coalescence with a fracture surface that contained multiple, large dimples. Alternatively, the 5N-Al wire failed by necking to a point with a fracture surface that contained a handful of small dimples. Figure 2 also demonstrates, though, that the post-DRX grain size in the 4N-Al wire was at least an order of magnitude smaller than that in the 5N-Al wire. For a single 4N-Al sheet material, Noell *et al.* [20] demonstrated that both the dimple density on the fracture surface and the failure mechanism depends on the grain size. In particular, samples with ~100 grains in the center of the neck failed by void coalescence, while samples with ~5 grains in the center of the neck failed by necking to a point. Thus, we propose that differences in grain size rather than purity between the 4N-Al and 5N-Al wires may be responsible for differences in dimple density on the fracture surface. This hypothesis is now considered in more detail.

Because voids in Al nucleate exclusively at dislocation boundaries, it is probable that the density of incipient voids in the specimen depends on the density of dislocation boundaries in the specimen. In Al, dislocation

boundaries primarily form near grain boundaries and grain boundary triple points [36]. For a given strain, the density of dislocation boundaries within a sample will thus increase as the density of grain boundaries increases, *i.e.* as the grain size decreases. By this argument, voids will nucleate more readily in the fine-grained (~10 μm) 4N-Al wire than the coarse-grained (~100 μm) 5N-Al wire. Hence, we propose that the observed differences between the 4N-Al and 5N-Al wires are likely best explained in terms of grain size rather than purity.

4.2 Void nucleation, dislocation density, and the hydrostatic stress

Perhaps the most surprising aspect of this study was the observation that voids nucleated after DRX rather than before. Two mechanisms for void nucleation in inclusion-free materials, such as the 4N-Al sheet material, have been proposed:

1. voids nucleate to relieve the local elastic stress produced by excess dislocations (*e.g.* dislocation pile-ups and dislocation boundaries) [1, 37-39], and
2. voids nucleate by vacancy condensation [17].

According to both mechanisms, the likelihood for void nucleation increases with increasing dislocation density [17, 38]. However, comparing Figure 1 and Figure 7 indicates that the dislocation density at void nucleation was even lower than that in the as-received material. Because DRX depends on attaining a critical dislocation density [33], it is reasonable to conclude that the dislocation density immediately before DRX was even larger than that in the as-received material and thus significantly greater than that at void nucleation. Why then did voids appear after DRX rather than before it?

In addition to the dislocation density, another important difference between the conditions at 90% and 15% of the UTS, *i.e.* before DRX and after void nucleation began, is the hydrostatic stress state. This affects void nucleation in several ways (as discussed in the next paragraph). Because the specimen necked significantly after DRX occurred, the hydrostatic stresses became significantly elevated. The hydrostatic stress in the center of the neck can be estimated using the Bridgman [40] equation,

$$\frac{\sigma_m}{Y} = \frac{1}{3} + \ln\left(\frac{a + 2R}{2R}\right) \quad 1$$

where $\frac{\sigma_m}{Y}$ is the stress triaxiality, a is the cross-sectional radius at the neck, and R is the neck radius. R was estimated from DIC images by fitting a cylinder to the necked region using polynomial surface fitting in MATLAB. These data suggest that the stress triaxiality when DRX began, when DRX ended, and when void nucleation began were approximately 0.37, 0.42, and 0.77, respectively. This latter value (0.77) is a conservative estimate for the stress triaxiality at void nucleation; the neck was asymmetrical, with a significantly larger radius R on one side than the other. The value of 0.77 was calculated using this maximum value of R. Using the minimum value of R provides a stress triaxiality of 1.25 at void nucleation.

It is hypothesized that hydrostatic stresses are critical to the early stages of void nucleation in pure metals for two reasons. First, hhydrostatic stresses provide a driving force that promotes vacancy aggregation into voids [41]. Second, studies of vacancy condensation in quenched aluminum have demonstrated that vacancy clusters collapse into dislocation loops or stacking fault tetrahedra unless they are stabilized [42-45]. During plastic deformation, the work applied by the hydrostatic stress is the likeliest stabilization mechanism for vacancy clusters [46]. Void nucleation may thus have been delayed until the hydrostatic stress produced by the neck was sufficiently large to stabilize critical void nuclei.

Hydrostatic stresses may also be important to the failure of Al specimens because they control the void growth rate, thereby affecting the ability for voids to grow large enough to coalesce. For example, according to the well-known Rice-Tracey relation [47], the void growth rate varies exponentially with the hydrostatic stress as

$$\frac{\dot{r}}{r} = \alpha \exp\left(\frac{3\sigma_m}{2Y}\right)\dot{\varepsilon}^{eq}. \qquad 2$$

where r is the void radius, $\dot{\varepsilon}^{eq}$ is the von Mises equivalent strain rate, and α is a numerical constant. Using the estimated stress triaxialities, the relative void growth rates were $1X$, $1.1X$, and $1.8X$ for the points where DRX began, DRX ended, and void nucleation began. If the maximum stress triaxiality calculated at void nucleation is used, the relative void growth rate when void nucleation began was $3.7X$. Hence, the driving force for void growth was 2 to 4 times as high at 15% UTS, when mesoscale voids were first observed, than before DRX occurred. It is hypothesized that this was another factor that made it possible for voids to affect the rupture process at lower dislocation densities than those present immediately before DRX.

5 Conclusion

In summary, this study demonstrated that 2nd-phase particles are not necessary for void nucleation in high-purity FCC metals that deform by slip. This widely held assumption was primarily based on early studies of fracture in Al. In the present investigation, it was shown that void nucleation Al is impeded by dynamic recrystallization, which erases the microstructural features, *i.e.*, the dislocation boundaries, necessary for void nucleation. For voids to nucleate in Al, these boundaries must reform after DRX. These results, combined with other recent observations of ductile rupture in pure Ta, suggest that the same microstructural features, *i.e.,* dislocation boundaries, control void nucleation in all pure metals that deform by slip.

Acknowledgements

The authors would like to acknowledge Jay Carroll, Doug Medlin, Helena Jin, Joseph Michael, and Sharlotte Kramer for beneficial discussions. Also, the authors would like to acknowledge Todd Huber, John Laing, Brad Salzbrenner, Richard Grant, Sara Dickens, Alice Kilgo, Chad Taylor, Bonnie McKenzie, Celedonio Jaramillo, Christina Profazi, and Curtis Mowry for their exceptional experimental support. Brad L. Boyce and Philip J. Noell accessed computational and experimental resources at the Center for Integrated Nanotechnologies. This work was supported by the Laboratory Directed Research and Development program at Sandia National Laboratories, a multimission laboratory managed and operated by National Technology and Engineering

Solutions of Sandia, LLC., a wholly owned subsidiary of Honeywell International, Inc., for the U.S. Department of Energy's National Nuclear Security Administration under contract DE-NA-0003525. This paper describes objective technical results and analysis. Any subjective views or opinions that might be expressed in the paper do not necessarily represent the views of the U.S. Department of Energy or the United States Government.

6 References

1. Zener, C., *The micro-mechanism of fracture.* Fracturing of metals, 1948. **3**.
2. Stroh, A.N., *A theory of the fracture of metals.* Advances in Physics, 1957. **6**(24): p. 418-465.
3. Cottrell, A.H., *Dislocations and plastic flow in crystals.* 1953.
4. Cottrell, A.H., *Dislocation and Mechanical Properties of Crystals*, J. Fisher, et al., Editors. 1957, Wiley, New York. p. 509.
5. Cottrell, I., *AH (1959) Theoretical aspects of fracture.* BL Averbach, OK Felbeck, GT Hahn, and OA Thomas (OOs.), Fracture. MIT press, Cambridge. Massachusetts, USA, 1959: p. 20-45.
6. Tipper, C.F., *The fracture of metals.* Metallurgia, 1949. **39**(231): p. 133-137.
7. Puttick, K.E., *Ductile fracture in metals.* Philosophical magazine, 1959. **4**(44): p. 964-969.
8. Orowan, E., *Fracture and strength of solids.* Reports on progress in physics, 1949. **12**(1): p. 185.
9. Miller, D.R. and F.M.C. Besag. *Metallographic Studies of Ductile Fracture in High Purity Aluminium and Lead*. in *Proceedings 1st International Conference on Fracture, Sendai, 1965, Vol. II, Japan 1965*. 1965.
10. Chin, G.Y., W.F. Hosford, and W.A. Backofen, *Ductile fracture of aluminum.* Transactions of the Metallurgical Society of AIME, 1964. **230**(3): p. 437.
11. Beevers, C.J. and R.W.K. Honeycombe. *Ductile fracture of single crystals*. in *ICF0, Swampscott-MA (USA) 1959*. 1959.
12. Beevers, C.J. and R.W.K. Honeycombe, *The initiation of ductile fracture in pure metals.* Philosophical Magazine, 1962. **7**(77): p. 763-773.
13. Ghahremaninezhad, A. and K. Ravi-Chandar, *Ductile failure in polycrystalline OFHC copper.* International Journal of Solids and Structures, 2011. **48**(24): p. 3299-3311.
14. Thompson, A.W. and P.F. Weihrauch, *Ductile fracture: nucleation at inclusions.* Scripta Metallurgica, 1976. **10**(2): p. 205-210.
15. Garrison, W.M. and N.R. Moody, *Ductile fracture.* Journal of Physics and Chemistry of Solids, 1987. **48**(11): p. 1035-1074.
16. Boyce, B.L., et al., *The morphology of tensile failure in tantalum.* Metallurgical and Materials Transactions A, 2013. **44**(10): p. 4567-4580.
17. Noell, P., et al., *Do voids nucleate at grain boundaries during ductile rupture?* Acta Materialia, 2017. **137**: p. 103-114.
18. Bay, B., et al., *Overview no. 96 evolution of fcc deformation structures in polyslip.* Acta metallurgica et materialia, 1992. **40**(2): p. 205-219.
19. Hansen, N., *New discoveries in deformed metals.* Metallurgical and materials transactions A, 2001. **32**(12): p. 2917-2935.
20. Noell, P.J., J.D. Carroll, and B.L. Boyce, *The mechanisms of ductile rupture.* Acta Materialia, 2018. **161**: p. 83-98.
21. International, A., *Standard Test Method for Analysis of Aluminum and Aluminum Alloys by Inductively Coupled Plasma Atomic Emission Spectrometry (Performance Based Method).* Standard Designation E3061 - 17, ASTM International, West Conshohocken, PA.

22. International, A., *Standard Test Methods for Determining Average Grain Size, Standard Designation E 112–13*. 2013, ASTM International.
23. ASTM, W.C.U., *Standard, A. S. T. M. "E8. Standard test method for tension testing of metallic materials."* 2004.
24. HKL Channel 5, O.I.P., Oxon, United Kingdom.
25. Bachmann, F., R. Hielscher, and H. Schaeben. *Texture analysis with MTEX--free and open source software toolbox*. in *Solid State Phenomena*. 2010.
26. Pantleon, W., *Resolving the geometrically necessary dislocation content by conventional electron backscattering diffraction.* Scripta Materialia, 2008. **58**(11): p. 994-997.
27. Montheillet, F. and J. Le Coze, *Influence of purity on the dynamic recrystallization of metals and alloys.* physica status solidi (a), 2002. **189**(1): p. 51-58.
28. Skrotzki, W., et al., *Recrystallization of high-purity aluminium during equal channel angular pressing.* Acta Materialia, 2007. **55**(7): p. 2211-2218.
29. Burke, J. and D. Turnbull, *Recrystallization and grain growth.* Progress in metal physics, 1952. **3**: p. 220-292.
30. Noell, P.J. and E.M. Taleff, *Dynamic abnormal grain growth in refractory metals.* JOM, 2015. **67**(11): p. 2642-2645.
31. Worthington, D.L., et al., *Dynamic abnormal grain growth in molybdenum.* Metallurgical and Materials Transactions A, 2013. **44**(11): p. 5025-5038.
32. Pedrazas, N.A., et al., *Dynamic abnormal grain growth in tantalum.* Materials Science and Engineering: A, 2014. **610**: p. 76-84.
33. Humphreys, F.J. and M. Hatherly, *Recrystallization and related annealing phenomena*. 2012: Elsevier.
34. Wong, S., P.D. Hodgson, and P. Thomson, *Room temperature deformation and recrystallisation behaviour of lead and lead–tin alloys in torsion and plane strain compression.* Materials science and technology, 1999. **15**(6): p. 689-696.
35. Haessner, F. and J. Schmidt, *Recovery and recrystallization of different grades of high purity aluminium determined with a low temperature calorimeter.* Scripta metallurgica, 1988. **22**(12): p. 1917-1922.
36. Randle, V., N. Hansen, and D.J. Jensen, *The deformation behaviour of grain boundary regions in polycrystalline aluminium.* Philosophical Magazine A, 1996. **73**(2): p. 265-282.
37. Weertman, J., *Zener–Stroh crack, Zener–Hollomon parameter, and other topics.* Journal of applied physics, 1986. **60**(6): p. 1877-1887.
38. Wilsdorf, H.G.F., *The ductile fracture of metals: a microstructural viewpoint.* Materials Science and Engineering, 1983. **59**(1): p. 1-39.
39. Jagannadham, K. and H.G.F. Wilsdorf, *Low energy dislocation structures associated with cracks in ductile fracture.* Materials Science and Engineering, 1986. **81**: p. 273-292.
40. Bridgman, P.W., *Studies in large plastic flow and fracture*. Vol. 177. 1952: McGraw-Hill New York.
41. Hirth, J.P. and W.D. Nix, *Analysis of cavity nucleation in solids subjected to external and internal stresses.* Acta metallurgica, 1985. **33**(3): p. 359-368.
42. Hirsch, P.B., et al., *Dislocation loops in quenched aluminium.* Philosophical Magazine, 1958. **3**(32): p. 897-908.
43. Kiritani, M., *Formation of voids and dislocation loops in quenched aluminum.* Journal of the Physical Society of Japan, 1964. **19**(5): p. 618-631.
44. Shimomura, Y. and S. Yoshida, *Heterogeneous nucleation of voids in quenched aluminum.* Journal of the Physical Society of Japan, 1967. **22**(1): p. 319-331.
45. Shimomura, Y. and Y. Moritaki, *Formation of Voids in Pure Aluminum Quenched in Hydrogen Gas.* Japanese Journal of Applied Physics, 1981. **20**(10): p. 1787.
46. Riedel, H., *Fracture at high Temperatures*. 1987: Springer Verlag.
47. Rice, J.R. and D.M. Tracey, *On the ductile enlargement of voids in triaxial stress fields.* Journal of the

Mechanics and Physics of Solids, 1969. **17**(3): p. 201-217.